Eur. Phys. J. D **39**, 261–269 (2006)
DOI: 10.1140/epjd/e2006-00084-4

**THE EUROPEAN PHYSICAL JOURNAL D**

# Detection by two-photon ionization and magnetic trapping of cold $Rb_2$ triplet state molecules*

J. Lozeille[1], A. Fioretti[1,a], C. Gabbanini[1], Y. Huang[2], H.K. Pechkis[2], D. Wang[2], P.L. Gould[2], E.E. Eyler[2], W.C. Stwalley[2], M. Aymar[3], and O. Dulieu[3,b]

[1] Istituto per i Processi Chimico-Fisici del C.N.R., Via G.Moruzzi 1, 56127 Pisa, Italy
[2] Physics Department, University of Connecticut Storrs, CT 06269, USA
[3] Laboratoire Aimé Cotton, CNRS, Campus d'Orsay, 91405 Orsay Cedex, France

Received 29 September 2005 / Received in final form 24 January 2006
Published online 20 April 2006 – 

**Abstract.** We present detailed experimental spectra and accurate theoretical interpretation of resonance-enhanced two-photon ionization of ultracold rubidium molecules in the 14000–17000 $cm^{-1}$ transition energy range. The dimers are formed in a magneto-optical trap by photoassociation followed by radiative decay into the $a\,^3\Sigma_u^+$ lowest triplet state. The theoretical treatment of the process, which reproduces the main features of the spectra, takes into account the photoassociation and decay steps as well as the resonant ionization through the manifold of intermediate *gerade* states correlated to the 5S + 4D limit. In particular, the energy of the $v = 1$ level of the (2) $^3\Sigma_g^+$ potential well has been determined for the first time. In addition, a tight constraint has been put on the position of the $a\,^3\Sigma_u^+$ repulsive wall. Finally, magnetic trapping of rubidium molecules in the $a\,^3\Sigma_u^+$ state is demonstrated.

**PACS.** 32.80.Pj Optical cooling of atoms; trapping – 33.80.Ps Optical cooling of molecules; trapping – 33.20.-t Molecular spectra

## 1 Introduction

After the great development of atomic physics at ultralow temperatures, in recent years new techniques to produce cold [1,2] and ultracold ($T < 1$ mK) [3] molecules have been experimentally implemented. In particular the method of photoassociation (PA) of colliding atomic pairs followed by radiative decay allows the formation of molecules in their electronic ground state or their lowest metastable state at translational temperatures almost equal to the starting atomic ones. Homonuclear alkali molecules in the tens or hundreds of $\mu$K range have been produced [3–6] as well as heteronuclear alkali dimers [7,8]. Another technique that has been recently developed, magnetoassociation, exploits magnetic tuning of Feshbach resonances to couple pairs of ultracold atoms to bound molecular states. By this method the molecules are typically produced in the highest bound states and can be quantum degenerate if the starting atomic sample is a Bose-Einstein condensate or a degenerate Fermi gas [9]. These loosely bound molecules can be detected in different ways, such as imaging after backconversion into free atoms or RF spectroscopy [10].

In contrast to magnetoassociation, the PA process yields more tightly bound molecules, which can be efficiently detected only via photoionization and ion detection. In particular, resonance-enhanced multiphoton ionization (REMPI) of cold dimers into molecular ions has been demonstrated as an efficient, although destructive, process. Two-photon ionization can be enhanced by the resonant absorption of a photon into an intermediate excited molecular state. For cesium and rubidium dimers an efficient pathway to molecular ionization passes through the states correlated with the 6S + 5D and 5S + 4D asymptotes respectively. Some of these states have been studied at thermal energies when dealing with the so called "*diffuse bands*" [11], and at low temperature with the technique of He nanodroplets [12]. For cesium an accurate analysis of the REMPI spectra in the region of the diffuse bands has been performed by comparing the experimental spectra obtained at ultralow temperature with a theoretical modelling of the process [13]. This demonstrated that the photoionization of ultracold molecules can be used as an efficient spectroscopic tool for the investigation of fairly highly excited molecular states, giving access to the triplet manifold of alkali pairs which is not easily attainable with conventional spectroscopy.

* Two supplementary tables (Tabs. I and II) are only available in electronic form at `http://www.eurphysj.org`

[a] A. Fioretti aknowledges French CNRS for funding his present stay at Laboratoire Aimé Cotton.

[b] e-mail: `olivier.dulieu@lac.u-psud.fr`

Here we present experimental spectra of the molecular bands observed by detecting triplet $Rb_2$ molecules in the metastable $a\ ^3\Sigma_u^+$ state. These spectra are more extended and have slightly better resolution than those previously reported [5,16]. They are analyzed theoretically, starting from an adiabatic set of potential energy surfaces (PES) in which spin-orbit coupling has been introduced. Although the potential curves are perturbed in the considered region, the present analysis succeeds in reproducing the main experimental features, i.e. the vibrational line series and corresponding intensity patterns, although the rotational structure is unresolved. For the first time, the position of one of the lowest ($v = 1$) vibrational levels of the (2) $^3\Sigma_g^+(0_g^-)$ state, has been determined, providing a good prospect for the well-depth of this state, as well as the position of the repulsive wall of the lowest triplet state $a\ ^3\Sigma_u^+$. Our spectra also probe the detection of the $a\ ^3\Sigma_u^+$ state molecules with vibrational selectivity.

First we briefly review the experimental procedure in Section 2, and in Section 3 we describe the theoretical approach used to interpret the recorded spectra. Our two-photon ionization spectra are carefully analyzed and discussed in Section 4. Finally, magnetic trapping of metastable triplet rubidium dimers is demonstrated in Section 5.

## 2 Experiment

Two different experimental setups located in Storrs and Pisa have been used to produce and detect cold $Rb_2$ molecules. In both cases molecules are formed from cold atoms in magneto-optical traps (MOTs) through the processes of photoassociation and subsequent spontaneous decay.

The Storrs experiment is described in detail in reference [15]. In brief, a cw single-mode Ti:sapphire laser with an output power of $\gtrsim$400 mW photoassociates $^{85}$Rb atoms in a MOT into the $0_g^-$ (5S + 5P$_{1/2}$) state, which radiatively decays to produce molecules in the $a\ ^3\Sigma_u^+$ state. We remark that the $0_g^-$ (5S + 5P$_{1/2}$) state used for the Storrs work has a $R^{-6}$ van der Waals interaction potential, while the $0_g^-$ (5S + 5P$_{3/2}$) state used in the Pisa experiments has an $R^{-3}$ dipole-dipole long range dependence. The metastable $a$ state molecules are ionized by a pulsed dye laser with a bandwidth of 0.05 cm$^{-1}$, a Continuum ND6000 dye laser pumped by the second harmonic of a Nd:YAG laser with a 10 Hz repetition rate. Typical dye laser pulse energies are about 3 mJ, with a pulse duration of ∼6 ns. The dye laser beam is focused into the MOT with a diameter of about 1 mm. Various dyes (LDS 698, DCM, and Rhodamine 610) have been used to cover the entire region from 14000 to 17000 cm$^{-1}$, as indicated with a dashed box in Figure 1. The molecular ions are detected by a microchannel plate in conjunction with a boxcar averager, providing time-of-flight mass selectivity.

In Pisa the experiment runs in a MOT trapping a few times $10^7$ atoms of either $^{85}$ Rb or $^{87}$Rb isotope with temperature and density of about 90 $\mu$K and $3\times10^{10}$ cm$^{-3}$

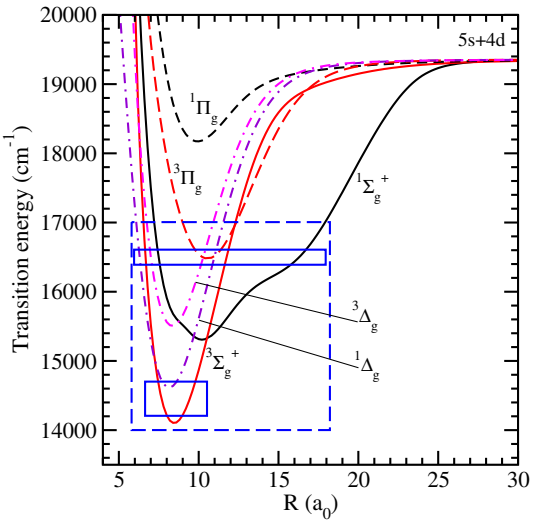


**Fig. 1.** Potential curves (without spin-orbit) of the rubidium dimer correlated to the 5S + 4D asymptote, relevant for the present study. Plain boxes indicate the energy range explored by the Pisa experiment, and dashed boxes by the Storrs experiment. A colour version of the figure is available in electronic form at `http://www.eurphysj.org`.

respectively. A diode laser photoassociates pairs of atoms into excited molecules. The diode laser is tuned to a high vibrational level ($v \approx 60$, bound by 1.1 cm$^{-1}$) of the shallow external well of the $0_g^-$ (5S + 5P$_{3/2}$) state that can spontaneously decay into the lowest triplet molecular state $a\ ^3\Sigma_u^+$ with a good branching ratio [5,16]. The diode laser, whose output power is 70 mW, is kept on resonance by stabilizing its frequency to an external Fabry-Perot interferometer; in this way the frequency is stabilized within a few MHz on the timescale of some minutes. The molecules thus produced are ionized by a dye laser with 5 ns pulse duration, spectral width 0.2 cm$^{-1}$ and up to 2 mJ of output energy operating with either LDS 698 dye or with a mixture of Rhodamine 610 and 640 dyes; the dye laser is pumped by the second harmonic of a Nd:YAG laser. The pulsed laser is gently focused into the MOT and is tuned to a molecular band connecting the lowest triplet state $a\ ^3\Sigma_u^+$ to the excited (2) $^3\Pi_g$ or (2) $^3\Sigma_g^+$ states correlated with the 5S + 4D asymptote within the two energy intervals 14200–14700 cm$^{-1}$ and 16400–16600 cm$^{-1}$ shown as plain boxes in Figure 1. The molecular ions are selected by time-of-flight and detected by a channeltron.

## 3 Theoretical treatment

As described above, we model here the following sequence of processes, neglecting the hyperfine structure of the atoms:

- photoassociation from the dissociation continuum of the $a\ ^3\Sigma_u^+$ state into bound levels of the $0_g^-$ (5S + 5P$_{1/2,3/2}$) states;
- spontaneous emission down to bound levels of the $a\ ^3\Sigma_u^+$ state;

- bound-bound transitions into levels of the dipole-allowed molecular states correlated to the 5S + $4D_{3/2,5/2}$ limits.

The present simulations of the REMPI spectra are achieved following the procedure described in reference [13], using the Mapped Fourier Grid Hamiltonian (MFGH) method which provides a convenient approach for the calculation of Franck-Condon factors involved in transition rates, especially for coupled electronic states. We assume that the PA step is performed at a fixed detuning $\delta_{PA}$ of the PA laser below the $(5S + 5P_{1/2,3/2})$ dissociation limits, so that the PA rate just represents a scaling factor for a given REMPI spectrum. A major difference between the two $0_g^-$ states when they are photoassociated occurs because of the different asymptotic behaviour of the surfaces at long range. As remarked before, the $0_g^-$ $(5S + 5P_{3/2})$ state scales asymptotically as $R^{-3}$, whereas the $0_g^-$ $(5S + 5P_{1/2})$ state scales as $R^{-6}$, so PA of the latter state occurs at much smaller range for a given detuning. The vibrational distribution of the $\Sigma_g^+$ cold molecules in the $a$ state is then determined by the decay probability of the photoassociated $0_g^-$ levels. We will see in the next section that the simulation predicts that the population of the $a$ state is confined in the uppermost vibrational states, with a binding energy smaller than 10 $cm^{-1}$. The computed REMPI spectra finally result from the absorption rate of these populated levels towards bound levels of the 5S + 4D manifold. Following reference [13] we assume that these latter levels are subsequently ionized with uniform probability, so that we ignore this last step in our model.

A previous study by some of the present authors [16] has determined the PES of the long range state $0_g^-$ $(5S + 5P_{3/2})$ of $^{87}Rb_2$ using a Rydberg-Klein-Rees (RKR) method and will be used in the present analysis ($D_e = 28.36$ $cm^{-1}$ $R_e \simeq 17$ Å). The long-range part of the $0_g^-$ $(5S + 5P_{1/2})$ state has been computed following the same perturbative procedure as in reference [14]. It provides a potential curve with a well depth $D_e = 3195.13$ $cm^{-1}$ and an equilibrium distance $R_e \simeq 9.75$ Å. The $a$ $^3\Sigma_u^+$ state potential curve is obtained from the calculations of reference [17], using for the Rb atoms the large basis of type B presented there. It is matched around $20a_0$ ($a_0 = 0.529177$ nm) to the usual long-range expansion $\Sigma_{n=6,8} C_n/R^n$, with $C_6 = 4691$ a.u. and $C_8 = 5.77 \times 10^5$ a.u. taken from the most recent data of references [18,19]. The repulsive wall of the curve is smoothly adjusted in order to reproduce the measured scattering length for this state, $a_T(^{85}Rb) = -369 \pm 16a_0$ and $a_T(^{87}Rb) = 106 \pm 4a_0$ [21]. The set of accessible potential curves of $g$ symmetry in Hund's case $a$, correlated to the 5S + 4D limit (see Fig. 1) is also taken from calculations of reference [17], using the type A basis. The adjustment of transition energies to the experimental values is performed by shifting these curves in energy. As suggested by the boxes in Figure 1, the long-range part of the potentials will not be involved in the computation of the bound-bound transition probabilities relevant for the REMPI spectra modelling. We also consider the dipole moment function for the transition between the $a$ state and the 5S + 4D manifold from our new calculations following the method of reference [17]. They are displayed in Figure 2 for the $^3\Sigma_g^+$ and $^3\Pi_g$ symmetries. Although their variation is quite important, they do not affect significantly the relative magnitude of the relevant dipole matrix elements of the transitions, which occur within a limited range of internuclear distances (see the boxes in Figs. 1 and 2). Moreover, the strongest transitions are saturated in the experiment, preventing an accurate analysis of the line intensities.

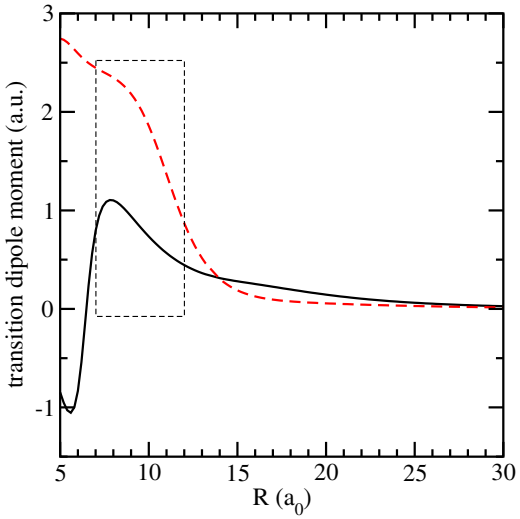


**Fig. 2.** Computed electric dipole transition moments of the rubidium dimer as a function of the internuclear distance. Full line: $a\ ^3\Sigma_u^+ \rightarrow (2)\ ^3\Sigma_g^+$ transition. Dashed line: $a\ ^3\Sigma_u^+ \rightarrow (2)^3\Pi_g$ transition. The box indicates the range of distances involved in the present analysis.

As Rb is a heavy atom, the spin-orbit interaction cannot be neglected. It couples the states displayed in Figure 1 to form Hund's case $c$ states, with symmetry $\Omega_g = 0_g^{+/-}$, $1_g$, $2_g$, $3_g$. In the framework of the Linear Combination of Atomic Orbitals (LCAO) approximation, the corresponding Hamiltonian matrices involve an interaction parameter $A_{4d} = (2/5)V_{SO}(4D)$, where $V_{SO}(4D)$ is the atomic spin-orbit splitting:

$$H(\Omega = 3) = (V(^3\Delta_g) + A_{4d}) \tag{1a}$$

$$H(\Omega = 2) = \begin{bmatrix} V(^3\Delta_g) & A_{4d} & A_{4d}/\sqrt{2} \\ A_{4d} & V(^1\Delta_g) & -A_{4d}/\sqrt{2} \\ A_{4d}/\sqrt{2} & -A_{4d}/\sqrt{2} & V(^3\Pi_g) \end{bmatrix} \tag{1b}$$

$$H(\Omega = 1) = \begin{bmatrix} V(^3\Delta_g) - A_{4d} & A_{4d}/\sqrt{2} & A_{4d}/\sqrt{2} & 0 \\ A_{4d}/\sqrt{2} & V(^3\Pi_g) & A_{4d}/2 & \sqrt{3}A_{4d}/2 \\ A_{4d}/\sqrt{2} & A_{4d}/2 & V(^1\Pi_g) & -\sqrt{3}A_{4d}/2 \\ 0 & \sqrt{3}A_{4d}/2 & -\sqrt{3}A_{4d}/2 & V(^3\Sigma_g^+) \end{bmatrix} \tag{1c}$$

**Table 1.** Initial value of effective spin-orbit interaction parameters used in the Hamiltonian matrices of equations (2b–2d). Final values obtained after the adjustment of the potential curves to reproduce line spacings are also reported. Only the symmetries for which the adjustment has been performed (i.e. $1_g$ and $0_g^{+/-}$, and not $2_g$) are described here.

| $\Omega$ | Diagonal parameters | | | Off-diagonal parameters | | |
|---|---|---|---|---|---|---|
| | | initial | final | | initial | final |
| $2_g$ | $A_2(^1\Delta_g)$ | –1 cm$^{-1}$ | - | $A_2(^3\Delta_g, ^3\Pi_g)$ | 5 cm$^{-1}$ | - |
| | $A_2(^3\Pi_g)$ | 95 cm$^{-1}$ | - | $A_2(^1\Delta_g, ^3\Pi_g)$ | 25 cm$^{-1}$ | - |
| $1_g$ | $A_1(^3\Delta_g)$ | –0.86 cm$^{-1}$ | –0.86 cm$^{-1}$ | $A_1(^3\Pi_g, ^3\Sigma_g^+)$ | 16.62 cm$^{-1}$ | 16.62 cm$^{-1}$ |
| | $A_1(^3\Pi_g)$ | –3 cm$^{-1}$ | –71.7 cm$^{-1}$ | | | |
| | $A_1(^3\Sigma_g^+)$ | 1.4 cm$^{-1}$ | 1.4 cm$^{-1}$ | | | |
| $0_g^-$ | $A_{0^-}(^3\Pi_g)$ | –90 cm$^{-1}$ | –151.1 cm$^{-1}$ | $A_{0^-}(^3\Pi_g, ^3\Sigma_g^+)$ | 20 cm$^{-1}$ | 9.62 cm$^{-1}$ |
| | $A_{0^-}(^3\Sigma_g^+)$ | 2 cm$^{-1}$ | –49.01 cm$^{-1}$ | | | |
| $0_g^+$ | $A_{0^+}(^3\Pi_g)$ | –95 cm$^{-1}$ | –161.1 cm$^{-1}$ | $A_{0^+}(^3\Pi_g, ^1\Sigma_g^+)$ | –0.38 cm$^{-1}$ | 9.62 cm$^{-1}$ |
| | $A_{0^+}(^1\Sigma_g^+)$ | –1 cm$^{-1}$ | –30 cm$^{-1}$ | | | |

$$H(\Omega=0^-)=\begin{bmatrix} V(^3\Pi_g)-A_{4d}/2 & \sqrt{3/2}A_{4d} \\ \sqrt{3/2}A_{4d} & V(^3\Sigma_g^+)\end{bmatrix} \quad (1d)$$

$$H(\Omega=0^+)=\begin{bmatrix} V(^3\Pi_g)-A_{4d}/2 & \sqrt{3/2}A_{4d} \\ \sqrt{3/2}A_{4d} & V(^1\Sigma_g^+)\end{bmatrix}. \quad (1e)$$

$$H'(\Omega=0^-)=\begin{bmatrix} V'_{0^-}(^3\Pi_g) & A_{0^-}(^3\Pi_g, ^3\Sigma_g^+) \\ A_{0^-}(^3\Pi_g, ^3\Sigma_g^+) & V'_{0^-}(^3\Sigma_g^+)\end{bmatrix} \quad (2c)$$

$$H'(\Omega=0^+)=\begin{bmatrix} V'_{0^+}(^3\Pi_g) & A_{0^+}(^3\Pi_g, ^1\Sigma_g^+) \\ A_{0^+}(^3\Pi_g, ^1\Sigma_g^+) & V'_{0^+}(^1\Sigma_g^+)\end{bmatrix} \quad (2d)$$

We do not include the rotation in the Hamiltonian, as the rotational structure is not resolved in the spectra.

The fine structure of the $4d$ atomic state in rubidium is very small, about $V_{SO}(4d) = 0.44$ cm$^{-1}$, but the molecular fine structure is expected to increase due to the electronic configuration mixing (for instance with the $5p$ state) in the distance range shown in Figure 1. As no data on molecular spin-orbit coupling are available in the literature, we assume that a set of $R$-independent molecular spin-orbit parameters is sufficient to reproduce the present experimental spectra. A strict analysis would require that these parameters converge toward their atomic value reported in equations (1a–1e) when $R \to \infty$, but as already mentioned, the long distance range is not important for the present study.

For each of the $0_g^{+/-}$, $1_g$, $2_g$ symmetries, we replace the matrices of equations (1b–1e) by the following ones involving effective potentials and effective symmetry-dependent interaction parameters:

$$H'(\Omega=2)=\begin{bmatrix} V'_2(^3\Delta_g) & A_{4d} & A_2(^3\Delta_g, ^3\Pi_g) \\ A_{4d} & V'_2(^1\Delta_g) & -A_2(^1\Delta_g, ^3\Pi_g) \\ A_2(^3\Delta_g, ^3\Pi_g) & -A_2(^1\Delta_g, ^3\Pi_g) & V'_2(^3\Pi_g)\end{bmatrix} \quad (2a)$$

$$H'(\Omega=1)=\begin{bmatrix} V'_1(^3\Delta_g) & A_{4d}/\sqrt{2} & A_{4d}/\sqrt{2} & 0 \\ A_{4d}/\sqrt{2} & V'_1(^3\Pi_g) & A_{4d}/\sqrt{2} & A_1(^3\Pi_g, ^3\Sigma_g^+) \\ A_{4d}/\sqrt{2} & A_{4d}/\sqrt{2} & V'_1(^1\Pi_g) & -\sqrt{3}A_{4d}/2 \\ 0 & A_1(^3\Pi_g, ^3\Sigma_g^+) & -\sqrt{3}A_{4d}/2 & V'_1(^3\Sigma_g^+)\end{bmatrix} \quad (2b)$$

where $V'_\Omega(\Lambda) = V(\Lambda) + \Delta_\Omega(\Lambda)$ for the symmetry $\Lambda$ in each of the subspaces $\Omega = 0_g^{+/-}$, $1_g$, $2_g$. The $V(\Lambda)$ potentials are taken from the computations described in reference [17], using the basis A defined in that paper. For completeness, these potentials are provided as supplementary material to the present paper, and can be obtained from the editor. The initial value of the parameters, reported in Table 1, are adjusted in order to match as closely as possible, after the diagonalization of the above matrices, the potential curves including spin-orbit interaction of reference [20] in the range of internuclear distances covered by the boxes in Figure 1. More specifically, we extract the effective coupling parameters from the magnitude of the avoided crossing between the fully adiabatic curves of Allouche [20]. When no avoided crossing is visible, the parameters are left equal to zero, and the optimization relies only on the shift of our initial potential curves. As expected the coupling between the $^3\Pi_g$ and $^3\Sigma_g^+$ states is almost the same for $0_g^-$ and $1_g$ symmetries. Also the $^3\Pi_g$ triplet manifold is split symmetrically around the $\Omega = 1$ component.

Our MFGH code solves coupled equations defined by the Hamiltonian matrix above, where the spin-orbit interaction is not diagonalized. The set of initial parameters in Table 1 are then used to start our simulations, and are modified as reported in Table 1 in order to match as closely as possible the spacings between experimental lines and the transition energies. We see that several parameters have changed quite a lot, which reveal that the initial set of potentials has to be lowered in energy, especially for the $^3\Pi_g$ and $^3\Sigma_g^+$ symmetries.

The effects of the coupling can be anticipated by looking at the potential energy curves. In addition to the $^3\Sigma_g^+$ state, $^1\Delta_g$ and $^3\Delta_g$ states also cross the $^3\Pi_g$ potential curve close to its minimum. Hence, coupled states are

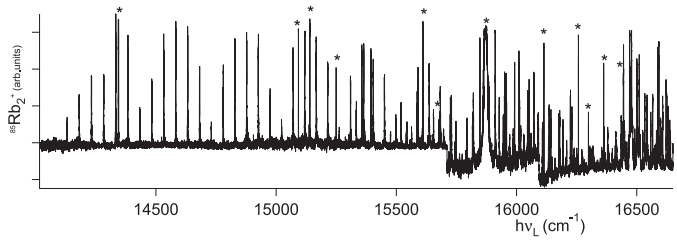


**Fig. 3.** Experimental REMPI spectrum of $^{85}Rb_2$ dimers produced by PA with detuning $\delta_{PA} = -69$ cm$^{-1}$ from the $(5S + 5P_{1/2})$ asymptote. The shift of the baseline is due to the change of the dye used for the ionization laser. The asterisks indicate ghost lines produced by two-photon transitions to atomic Rydberg states, which saturate the microchannel plate sufficiently to produce signals at the time of flight of the molecular ions.

expected to appear in the upper part of the recorded experimental spectra.

## 4 Interpretation of the two-photon ionization spectra

The ion spectra recorded at Storrs for $^{85}Rb_2$ dimers are shown in Figure 3, when the $0_g^-$ $(5S + 5P_{1/2})$ state is photoassociated at a detuning $\delta_{PA} = -69$ cm$^{-1}$. These spectra encompass the entire region from 14000 to 17000 cm$^{-1}$, including also the frequency range not covered by the spectra of references [5,16]. In the low frequency region the ionization pathway is due exclusively to the intermediate (2) $^3\Sigma_g^+$ molecular state. By using the procedure described in Section 3, the formation of cold molecules is computed from PA through the $0_g^-$ $(5S + 5P_{1/2})$ state and radiative decay into the metastable triplet state $a\ ^3\Sigma_u^+$.

The expected vibrational distribution of the cold molecules created in the $a$ state can be characterized by looking at Figure 4. Due to the shorter range of the $0_g^-(5S + 5P_{1/2})$ state relative to the $0_g^-(5S + 5P_{3/2})$ state, the $0_g^- \rightarrow a$ decay is expected to populate a larger number of bound levels in the $a$ state in the former case than in the latter. However, our calculations show that Franck-Condon factors for the $0_g^-(5S + 5P_{1/2}) \rightarrow a$ transition are significant only for a narrow binding energy range of about 1 cm$^{-1}$, corresponding to 4 levels of the $a$ state, (see Fig. 4a), and for a somewhat larger range for the $0_g^-(5S + 5P_{3/2}) \rightarrow a$ transition, close to 10 cm$^{-1}$, corresponding to 8 levels of the $a$ state (see Figs. 4b and 4c). The explanation relies on the presence of a potential barrier at intermediate distances between the two wells off the $0_g^-(5S + 5P_{3/2})$ potential, which allows larger FC factors with more deeply bound $a$ levels.

The analysis of the detection spectrum starts with the theoretical potentials of the $a\ ^3\Sigma_u^+$ and (2) $^3\Sigma_g^+$ states. We first vary the parameters of the $0_g^-$ Hamiltonian matrix to match the line spacings (see values reported in Tab. 1). Then we slightly modify the position of the $a\ ^3\Sigma_u^+$ repulsive wall such that the inner turning point at the dissociation energy is moved from the computed position of $9.44a_0$ to $9.12a_0$, in order to match the intensity distribution of the experimental spectrum (Fig. 5). The computed line spacings actually match very well the experimental ones, as can be seen in Figure 6. The computed Franck-Condon factors are in reasonable agreement with the recorded intensities, given that there is considerable saturation of the bound-bound transitions in the experiment, causing the intensity minima to be less pronounced than in the simulation and giving an impression of mismatch near transition energies 14470, 14950, and 15200 cm$^{-1}$. In addition, there are discontinuities in the absolute amplitude of the experimental ion signal corresponding to changes of the laser dye. The obtained agreement provides a strong experimental constraint on the position of this wall. We note that the scattering length also changes with this adjustment, but this will affect only the long-range part of the wave function of the highest vibrational levels, not relevant in the present calculations. In other words, such an intensity matching yields information which affects only for the position of the repulsive wall. The simulation indicates that the first observed line at 14128.4 cm$^{-1}$ should correspond

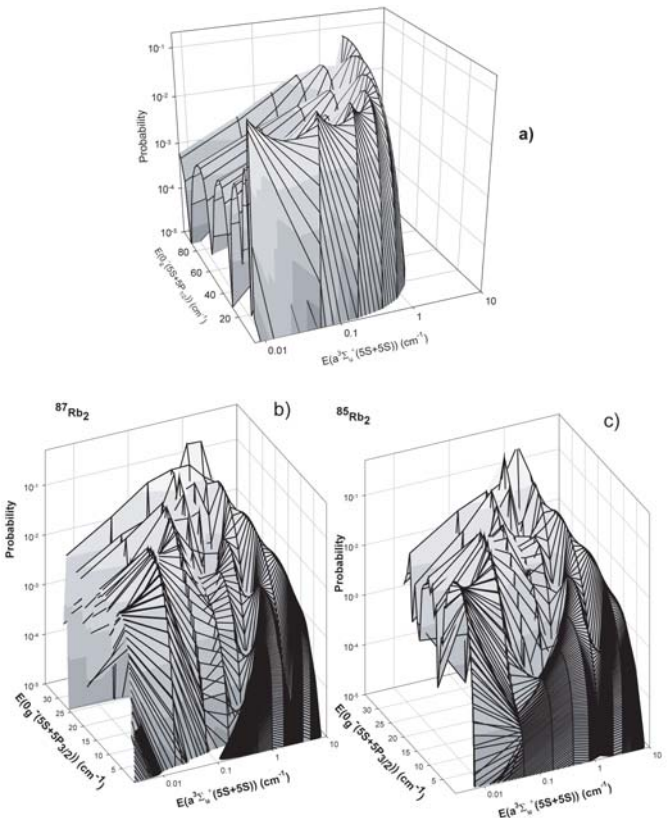


**Fig. 4.** Computed Franck-Condon factors of the uppermost vibrational levels of the $a\ ^3\Sigma_u^+$ metastable state with levels of the $0_g^-$ excited states, as functions of their binding energy expressed in cm$^{-1}$ (on a logarithmic scale for the $a$ levels). (a) For the $^{85}Rb_2$ molecule photoassociated in the $0_g^-$ $(5S+5P_{1/2})$ state. (b) For the $^{87}Rb_2$ molecule photoassociated in the $0_g^-$ $(5S+5P_{3/2})$ state. (c) For the $^{85}Rb_2$ molecule photoassociated in the $0_g^-$ $(5S + 5P_{3/2})$ state.

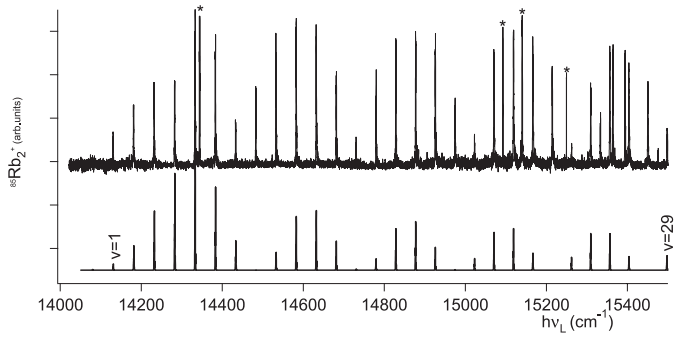


**Fig. 5.** Computed Franck-Condon factors for the vibrational levels of the (2) $^3\Sigma_g^+$ state with the $a$ $^3\Sigma_u^+$ levels in $^{85}Rb_2$ (lower graph), characterizing the transitions detected in the low energy part of the REMPI spectrum (for $\delta_{PA}(5S + 5P_{1/2}) = -69$ cm$^{-1}$) of Figure 3 (upper graph). Lines produced by atomic transitions are denoted with an asterisk. The assigned energy position of the $v = 1$ level of the (2) $^3\Sigma_g^+$ state is reported.

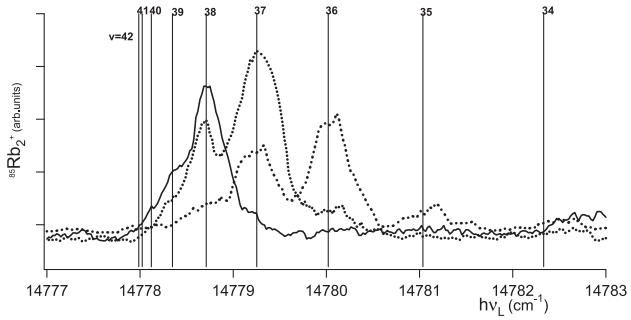


**Fig. 7.** Blow-up of a REMPI spectrum around 14779 cm$^{-1}$, for different detunings of the $0_g^-$ (5S + 5P$_{1/2}$) state: $\delta_{PA} = -69$ cm$^{-1}$ (dashed line), –43 cm$^{-1}$ (dotted line), –17 cm$^{-1}$ (full line). The ionization of the $a$ levels proceeds through the same intermediate level of the first REMPI step. The assignment of the vibrational levels in the ground $a$ $^3\Sigma_u^+$ state is shown. Note that the vibrational index is arbitrary here (see text).

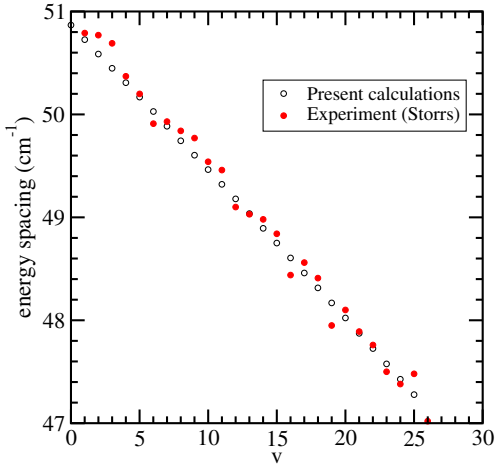


**Fig. 6.** Energy spacing of the computed vibrational levels of the adjusted (2) $^3\Sigma_g^+$ state (open circles) compared to the energy spacing of the assigned lines in Figure 5 (full circles).

to ionization through the $v = 1$ level of the (2) $^3\Sigma_g^+$ state, while the $v = 0$ level would not be observed. This provides an important objective for a further spectroscopic determination of the entire potential well.

The present resolution allows also for state-selective detection of the cold dimers. In Figure 7 we report three high resolution detection spectra at different PA laser detunings with respect to the 5S + 5P$_{1/2}$ asymptote where we can identify the populated vibrational levels in the $a$ $^3\Sigma_u^+$ state. Note that the vibrational indexes in Figure 7 are arbitrary: indeed, we built the $a$ potential from our computed potential matched at large distances to reliable long-range coefficients. The vibrational spacing is expected to be well reproduced, but as we moved the repulsive wall during the simulations, the scattering length is then slightly changed, as well as the absolute position of the uppermost vibrational levels. Moreover we neglect the rotational structure of the vibrational levels involved in the transitions as it is unresolved in the experimental spectra. The agreement of the computed lines with the experimental signals is obtained by shifting the former by 0.22 cm$^{-1}$, which in any case remains within the experimental reproducibility. We emphasize that such a state selectivity is an important diagnostic for future experiments in population transfer and state-selective ultracold chemistry.

When using higher frequencies for the pulsed dye laser, i.e. addressing transition energies larger than 16300 cm$^{-1}$, the ionization pathway occurs in a region where the (2) $^3\Sigma_g^+$, (2) $^3\Pi_g$, (1) $^3\Delta_g$ and (3) $^1\Sigma_g^+$ states are all present, and may be efficiently coupled by the spin-orbit interaction. The spectrum displayed in Figure 8 is indeed more complicated than in the previous case. Several broad atomic lines are still present, and overlap other lines. There is also a significant power broadening effect, which was not so crucial in Figure 5 where the density of lines was lower. The assignment achieved in Figure 5 for the (2) $^3\Sigma_g^+$ levels between 14000 and 15300 cm$^{-1}$, allows to use reliable parameters to start the simulations. We can actually identify (2) $^3\Sigma_g^+$ lines throughout the spectral range between the zones covered in Figures 5 and 8. In contrast with the previous case, it is tedious here to rely on the line intensities to assign unambiguously the vibrational numbering of the (2) $^3\Pi_g$ fine structure components. Relying on line spacings, we tentatively label the lines located at 16344 cm$^{-1}$ and 16425 cm$^{-1}$ as being due to the $v = 0$ levels of the $0_g^-$ and $1_g$ components of the (2) $^3\Pi_g$ state, separated by 81 cm$^{-1}$. Several (2) $^3\Pi_g(0_g^-)$ and (2) $^3\Pi_g(0_g^+)$ doublets of lines are also visible, separated by about 9 cm$^{-1}$.

The computed positions of the (1) $^3\Delta_g(1_g)$ and (2) $^1\Sigma_g^+(0_g^+)$ lines are also reported for completness, although they do not match measured lines at the present status of our simulations. However the corresponding levels are coupled via spin-orbit to the

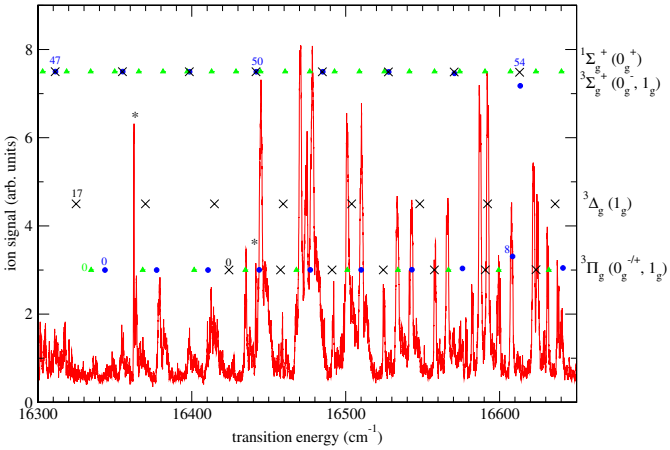


**Fig. 8.** Recorded ion signal from Storrs experiment, in the energy region where the (2) $^3\Pi_g$ manifold is expected to be populated. Tentative assignments are reported, following our coupled state calculations described in the text. The baseline of the symbols is arbitrary, helping the eye to distinguish among the components. All reported levels but one are found unperturbed, and can be easily assigned to Hund's case (a) states, as follows: full (blue) circles: $0_g^-$ ($^3\Sigma_g^+$, $^3\Pi_g$) series, full (green) triangles: $0_g^+$ ($^1\Sigma_g^+$, $^3\Pi_g$); crosses: $1_g$ ($^3\Sigma_g^+$, $^3\Pi_g$, $^3\Delta_g$) series. The only predicted perturbation occurs around 16610 $cm^{-1}$ in the $0_g^-$ symmetry, between $v = 8$ of $^3\Pi_g$ and $v = 54$ of $^3\Sigma_g^+$. Several atomic lines are also identified, and marked with asterisks. A colour version of the figure is available in electronic form at `http://www.eurphysj.org`.

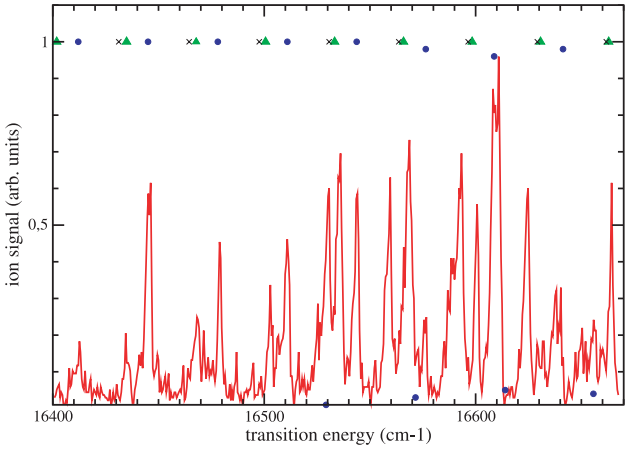


**Fig. 9.** Experimental ion spectrum recorded in Pisa during the detection of cold $^{87}Rb_2$ dimers, after photoassociation of the $0_g^-$ ($5S + 5P_{3/2}$) state. Coloured symbols indicate the present tentative assignment of the three series associated to the (2) $^3\Pi_g$ $0_g^-$ (full blue circles), $0_g^+$ (green triangles), $1_g$(crosses). The first symbol visible in this energy range corresponds to $v = 2$, $v = 2$, and $v = 0$ for the (2) $^3\Pi_g$ $0_g^-$, $0_g^+$, and $1_g$ components respectively. The magnitude of the computed line intensities have been arbitrarily taken equal to unity, which expresses that the spin-orbit coupling implemented in the model has no effect, except for the blue circle series: the symbols close to zero are associated to (2) $^3\Sigma_g^+$ $0_g^-$ levels, slightly coupled to the (2) $^3\Pi_g$ $0_g^-$ levels. A colour version of the figure is available in electronic form at `http://www.eurphysj.org`.

(2) $^3\Pi_g$ and (2) $^3\Sigma_g^+$ components. We note that a first series of lines not belonging to the (2) $^3\Sigma_g^+(0_g^-)$ series actually starts at 15333 $cm^{-1}$, i.e. close to the bottom of the (2) $^1\Sigma_g^+(0_g^+)$ potential well (see Fig. 1). Similarly, another unassigned series seems to start around 15500 $cm^{-1}$, corresponding to the energy of the bottom of the (1) $^3\Delta_g(1_g)$ potential well. These features are still under investigation in our groups. Finally, the region from 16650 to 17000 $cm^{-1}$ becomes too perturbed to allow reliable assignments of the transitions.

The same procedure has been applied to simulate the detection of $^{87}Rb_2$ dimers performed in Pisa. In this case the cold molecules are formed by PA into the $v = 60$ level ($\delta_{PA} = -1.1$ $cm^{-1}$) of the $0_g^-$ ($5S + 5P_{3/2}$) state and radiative decay into the $a\ ^3\Sigma_u^+$ state. Even if the final vibrational distribution in the $a$ state is not identical to the one yielded by the Storrs experiment, the detection spectrum should look roughly similar in the same spectral region. The experimental spectrum, which indeed looks complicated, is shown in Figure 9, together with the results of our computations. We performed a coupled state calculation without adjusting the coupling parameters, as the energy range of the measurement was not large enough. Then we assigned the levels by shifting the (2) $^3\Pi_g$ components to match the resulting energy spectrum to the experimental one. The (2) $^3\Pi_g(0_g^-)$ and (2) $^3\Pi_g(0_g^+)$ doublets can be identified. As previously, this is not so obvious for the (2) $^3\Pi_g(1_g)$ series.

## 5 Magnetic trapping of the triplet molecules

Recently, triplet $Rb_2$ molecules produced by photoassociation have been optically trapped [24]. Because triplet molecules have a magnetic moment, they can also be magnetically trapped [22,23]. The inhomogeneous magnetic field of our MOT forms a sufficiently deep magnetic trap to confine a fraction of the triplet $Rb_2$ molecules produced by PA. The combined magnetic and gravitational potentials are shown in Figure 10. Assuming a dipole moment of $2\mu_B$ (where $\mu_B = 9.27 \times 10^{-24}$ J/T is the Bohr magneton), the vertical (axial) magnetic field gradient of 28 G/cm provides a maximum trapping force, expressed in temperature units, of 3.8 mK/cm, almost twice the gravitational force of 2.0 mK/cm. The maximum horizontal (radial) trapping force is 1.9 mK/cm. The maximum magnetic force occurs only for those weak-field-seeking molecules that have the most negative projection of magnetic dipole moment on the local field. Since the Rb atoms in the MOT are unpolarized, we expect that the triplet molecules formed by PA will have a distribution of dipole moment projections and therefore only a fraction of them (∼20%) will experience a sufficiently large trapping force to overcome gravity. Because even the maximum trapping force is rather weak, the trapped molecules will occupy a volume considerably larger than that sampled by the detection laser. Trapping is verified by turning off the PA laser and delaying the detection. For sufficiently long delays (>30 ms), untrapped

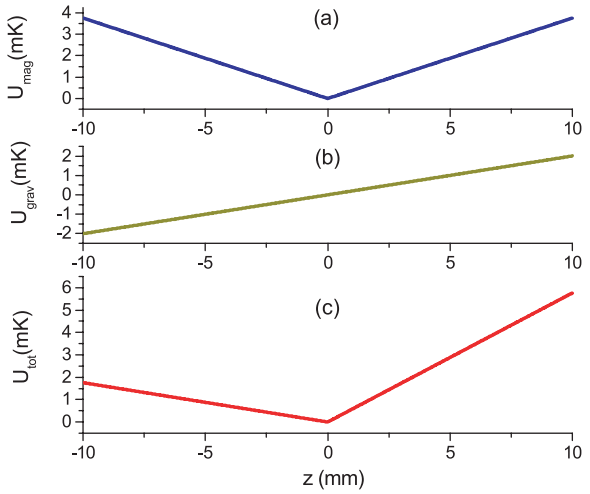


**Fig. 10.** Magnetic trapping potential for $Rb_2$ triplet molecules. (a) Dependence of the magnetic potential energy on vertical coordinate $z$ for a vertical magnetic field gradient of 28 G/cm. The maximum trapping force (magnetic dipole moment projection of $-2\mu_B$) is assumed. (b) Gravitational potential energy. (c) Total potential energy, i.e., the sum of (a) and (b).

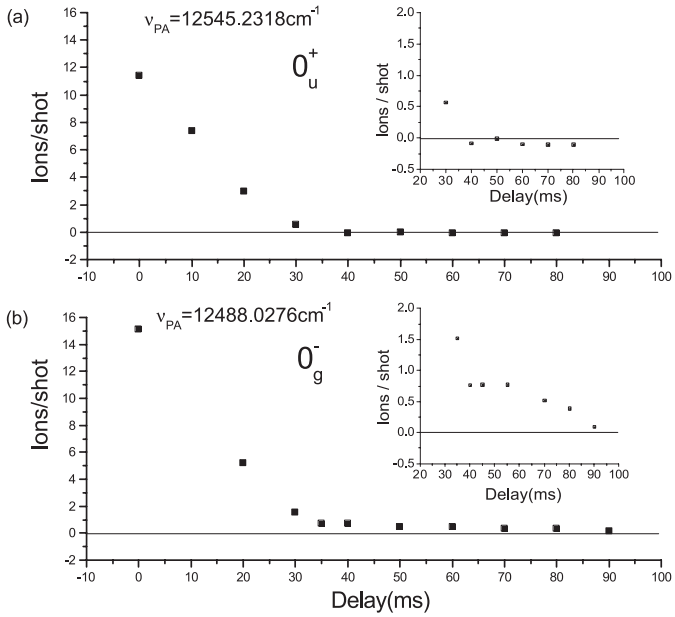


**Fig. 11.** Ion signal as a function of delay between turning off the PA laser and the detection pulse. In (a), PA to the $0^+_u$ state ($\delta_{PA}$ = –33.75 cm$^{-1}$) is used, resulting in $X\ ^1\Sigma^+_g$ molecules, which are not trapped. In (b), PA to the $0^-_g$ state ($\delta_{PA}$ = –90.95 cm$^{-1}$) is used, resulting in a $a\ ^3\Sigma^+_u$ molecules, a fraction of which are trapped. The insets depict the data at long delay times with an expanded vertical scale.

molecules will have left the detection region through a combination of ballistic motion and gravity. For the data shown in Figure 11b, PA takes place via the $0^-_g$ state, which decays exclusively to the $a$ state. The signal at long delays is due to the fraction of trapped triplet molecules which find themselves in the detection volume when the detection laser fires. In contrast, when PA to the $0^+_u$ state is used, the decay is to the $X\ ^1\Sigma^+_g$ state. Since singlet states have negligibly small magnetic moments, these $X$ state molecules are not trapped, resulting in an absence of signal at long delays, as shown in Figure 11a.

## 6 Summary

We have presented detailed experimental spectra in the 14000–17000 cm$^{-1}$ range and an accurate theoretical analysis of the REMPI ionization process of ultracold $Rb_2$ molecules produced in a magneto-optical trap. The analysis is based on the adiabatic set of potential energy surfaces for the states correlated to the (5S + 4D) asymptote of Rb. The simulation, together with experimental spectra that are more extended and at higher resolution than those previously published, allows us to identify the main features of the ionization channels and to state-selectively detect the cold dimers. In particular, we are able to reproduce accurately ionization spectra through the (2) $^3\Sigma^+_g$ intermediate state, of which we determine the absolute position of the $v = 1$ vibrational level. More qualitative agreement is obtained in the analysis of the ionization process through the (2) $^3\Pi_g$ state. Moreover, our simulations allow us to determine the position of the inner repulsive wall of the $a\ ^3\Sigma^+_u$ ground molecular state. Finally, evidence of magnetic trapping of ultracold rubidium molecules in their triplet ground state is demonstrated.

In perspective, the state selective ionization of ground state molecules demonstrated here will be a powerful tool for future investigation of level-dependent molecular properties and for optical pumping of cold molecules into more deeply bound vibrational levels of the ground state.

This work is supported by the European Research and Training Network (RTN) *Cold Molecules* (HPRN-CT-2002-00290, Pisa, Orsay) and by the U.S. National Science Foundation (Storrs), which also funded U.S. participation in the RTN Cold Molecules Network. We gratefully acknowledge A.R. Allouche and M. Aubert-Frécon for providing the fully adiabatic potential curves including fine structure, and A. Rizzo and F. Spiegelman for helpful discussions.

## References

1. J.D. Weinstein, R. de Carvalho, T. Guillet, B. Friedrich, J.M. Doyle, Nature **395**, 148 (1998)
2. H.L. Bethlem, G. Berden, G. Meijer, Phys. Rev. Lett. **83**, 1558 (1999)
3. A. Fioretti, D. Comparat, A. Crubellier, O. Dulieu, F. Masnou-Seeuws, P. Pillet, Phys. Rev. Lett. **80**, 4402 (1998)
4. A.N. Nikolov, E.E. Eyler, X.T. Wang, H. Wang, W.C. Stwalley, P.L. Gould, Phys. Rev. Lett. **82**, 703 (1999)
5. C. Gabbanini, A. Fioretti, A. Lucchesini, S. Gozzini, M. Mazzoni, Phys. Rev. Lett. **84**, 2814 (2000)
6. F.K. Fatemi, K.M. Jones, P.D. Lett, E. Tiesinga, Phys. Rev. A **66**, 053401 (2002)

7. A.J. Kerman, J.M. Sage, S. Sainis, T. Bergeman, D. DeMille, Phys. Rev. Lett. **92**, 033004 (2004)
8. D. Wang, J. Qi, M.F. Stone, O. Nikolayeva, H. Wang, B. Hattaway, S.D. Gensemer, P.L. Gould, E.E. Eyler, W.C. Stwalley, Phys. Rev. Lett. **93**, 243005 (2004)
9. T. Weber, J. Herbig, M. Mark, H.C. Nagerl, R. Grimm, Science **299**, 232 (2003)
10. C.A. Regal, C. Ticknor, J.L. Bohn, D.S. Jin, Nature **424**, 47 (2003)
11. G. Pichler, S. Milosevic, D. Veza, R. Beuc, J. Phys. B **16**, 4619 (1983)
12. F.R. Bruhl, R.A. Miron, W.E. Ernst, J. Chem. Phys. **115**, 10275 (2001)
13. C.M. Dion, O. Dulieu, D. Comparat, W. de Souza Melo, N. Vanhaecke, P. Pillet, R. Beuc, S. Milosevic, G. Pichler, Eur. Phys. J. D **18**, 365 (2002)
14. C.M. Dion, C. Drag, O. Dulieu, B. Laburthe Tolra, F. Masnou-Seeuws, P. Pillet, Phys. Rev. Lett. **86**, 2253 (2001)
15. Y. Huang, J. Qi, H.K. Pechkis, D. Wang, E.E. Eyler, P.L. Gould, W.C. Stwalley, J. Phys. B (to be published)
16. A. Fioretti, C. Amiot, C.M. Dion, O. Dulieu, M. Mazzoni, G. Smirne, C. Gabbanini, Eur. Phys. J. D **15**, 189 (2001)
17. M. Aymar, O. Dulieu, J. Chem. Phys. **122**, 204302 (2005)
18. A. Derevianko, W.R. Johnson, M.S. Safronova, J.F. Babb, Phys. Rev. Lett. **82**, 3589 (1999)
19. S.G. Porsev, A. Derevianko, J. Chem. Phys. **119**, 844 (2003)
20. A.R. Allouche, M. Aubert-Frécon, private communication
21. J.L. Roberts, N.R. Claussen, J.P. Burke, C.H. Greene, E.A. Cornell, C.E. Wieman, Phys. Rev. Lett. **81**, 5109 (1998)
22. N. Vanhaecke, W. de Souza Melo, B.L. Tolra, D. Comparat, P. Pillet, Phys. Rev. Lett. **89**, 063001 (2002)
23. D. Wang, J. Qi, M.F. Stone, O. Nikolayeva, B. Hattaway, S.D. Gensemer, H. Wang, W.T. Zemke, P.L. Gould, E.E. Eyler, W.C. Stwalley, Eur. Phys. J. D **31**, 165 (2004)
24. A. Fioretti, J. Lozeille, C.A. Massa, M.C. Gabbanini, Opt. Commun. **243**, 203 (2004)